The Isostructural Substitution-Induced Growth Mechanism of Rutile TiO_2 Electron Transport Layer and the Dominant Distribution for Efficient Carbon-Based Perovskite Solar Cells

Yuan-Bo Yang, Peng Chen, Qian Zhao, Hong-Shi Li, Guo-Ran Li, and Xue-Ping Gao*

Rutile TiO_2 (R-TiO_2) produced by chemical bath deposition (CBD) is widely considered as the desired electron transport layer (ETL) for perovskite solar cells (PSCs). However, the understanding of the growth mechanism of R-TiO_2 ETL and its general regular pattern affecting power conversion efficiency (PCE) is underappreciated. Herein, the growth mechanism of TiO_2 on fluorine-doped SnO_2 substrate (FTO) is demonstrated and it is revealed that pure R-TiO_2, rather than a rutile/anatase mixed crystal, is formed under an Sn–Ti isostructural substitution effect. The similarity of lattice parameters and phase structure between FTO and R-TiO_2 can reduce interface misfit and nucleation barrier, thus boosting heterogeneous nucleation and growth of R-TiO_2 simultaneously. Based on the key growth conditions of the R-TiO_2 ETL, the dominant distribution of PCE for hole transport layer (HTL)-free carbon-based planar perovskite solar cells is illustrated and discussed, and a champion efficiency of 14.0% is achieved.

1. Introduction

Perovskite solar cells (PSCs) have shown remarkable breakthroughs in photovoltaic performance (>25%)[1] within around a decade, and are regarded as excellent candidates for future photovoltaic applications. Hole transport layer (HTL)-free carbon-based PSCs[2] are developed to reduce the costs mainly incurred inexpensive hole transport materials, noble metal counter electrode (Au or Ag), and corresponding time-consuming vacuum deposition.[3] Within such an HTL-free fluorine-doped SnO_2 substrate (FTO)/electron transport layer (ETL)/perovskite/carbon structure, ETL would be the only carrier-selective blocking layer for the whole device, which determines the stability and power conversion efficiency of PSCs.[4] Therefore, deep insights into ETL are the keys to constructing high-efficiency HTL-free carbon-based planar PSCs.

TiO_2, as the most successful ETL, is widely applied in third-generation solar cells (from dye-sensitized solar cells to recent PSCs).[5] TiO_2 generally comes in three crystalline polymorphs: anatase (A-TiO_2), brookite (B-TiO_2), and rutile (R-TiO_2) belonging to the tetragonal, orthorhombic, and tetragonal crystal system, respectively.[6] Thereinto, R-TiO_2 has the most stable crystal phase with appropriate band positions for PSCs, while high-temperature annealing (500–1000 °C) is usually needed to ensure structure transition from anatase or brookite phase to rutile phase. To avoid the high-temperature process, chemical bath deposition (CBD)[7] under mild thermal conditions is applied for R-TiO_2 ETL preparation. Gratzel and coworkers deposited a nanocrystalline rutile TiO_2 ETL on FTO conductive substrate via hydrolysis of $TiCl_4$ at 70 °C, demonstrating nanocrystalline R-TiO_2 played a more essential role in electron transfer in PSCs compared with A-TiO_2.[8] Hu et al. reported that R-TiO_2 ETL showed faster electron transfer, better interface contacting, and less defect density than that of A-TiO_2, and a power conversion efficiency (PCE) of 20.9% was delivered.[9] A low-temperature softcover-assisted hydrolysis method for R-TiO_2 was displayed by Han and coworkers,[10] which provided a novel idea on depositing large-area TiO_2 films for the fabrication of solar modules. As demonstrated earlier, in PSCs, numerous applications of R-TiO_2 prepared by the $TiCl_4$ hydrolysis are presented so far; however, the reason for the preference of rutile phase when growing TiO_2 on FTO surface is still unclear.[11] Moreover, it is difficult and sometimes confusing when one tries to find some general regular patterns of R-TiO_2 ETL preparation affecting the final performance of PSCs.

In this work, we shed light on the physicochemical process of selective deposition of R-TiO_2 on FTO surface and use an isostructural substitution-induced growth mechanism for the first time to explain in detail why only R-TiO_2 grows on the FTO surface while both A-TiO_2 and R-TiO_2 are produced in solution during the $TiCl_4$ hydrolysis process. Following this isostructural substitution-induced growth mechanism, the obtained pure R-TiO_2 ETL via CBD method supports the corresponding PSCs to reach PCE exceeding 13%, which is in the top range[12] for HTL-free carbon-based PSCs. Benefiting from the advantages of stable R-TiO_2 and HTL-free carbon-based construction, our

---

Y.-B. Yang, P. Chen, Q. Zhao, H.-S. Li, G.-R. Li, X.-P. Gao
Institute of New Energy Material Chemistry
School of Materials Science and Engineering
Renewable Energy Conversion and Storage Centre
Nankai University
Tianjin 300350, China
E-mail: guoranli@nankai.edu.cn

The ORCID identification number(s) for the author(s) of this article can be found under https://doi.org/10.1002/solr.202100307.

DOI: 10.1002/solr.202100307

devices also delivered high tolerance to extremely high temperatures for PSCs. Moreover, the dominant distribution of PCE for HTL-free carbon-based planar PSCs is illustrated, establishing a correlation between ETL preparation and PCE of PSCs.

2. Results and Discussion

The TiO_2 crystal type is mainly dependent on how Ti—O octahedrons are connected.[13] In A-TiO_2, Ti^{4+} is the core of TiO_6 octahedron that is connected with eight adjacent Ti—O octahedrons by four common edges and four common vertexes, forming a tetragonal structure. For R-TiO_2, the phase structure has a similar tetragonal unit cell to anatase, but the difference is that the rutile structure can be viewed as infinite columns of edge-sharing Ti—O octahedrons, among which each edge-shared oxygen is corner-shared with a neighboring infinite Ti—O octahedron chain.[14] In these three polymorphs, A-TiO_2 is commonly the first polymorph to obtain in synthesis processes because of the lower surface energy, while R-TiO_2 is the most thermodynamic stable crystal with an irreversible transformation from A-TiO_2 around 500–1000 °C.[15] During the $TiCl_4$ hydrolysis process in a highly acidic environment ($pH < 1$), A-TiO_2 and R-TiO_2 can both be formed as demonstrated in previous reports.[16] However, different from the homogeneous nucleation in solution, the formation of TiO_2 embryos on the FTO surface is a heterogeneous nucleation process with a lower nucleation barrier. Consequently, the nucleation and growth of TiO_2 are influenced by the surface of FTO with an exposed rutile SnO_2 structure. Considering fluorine-doped SnO_2 (the commercial FTO) belongs to the tetragonal system (Figure 2a), which has the same phase structure and close lattice parameter with R-TiO_2[17] ($a = b = 4.593$ $c = 2.959$ for R-TiO_2; $a = b = 4.75$ $c = 3.198$ for tetragonal SnO_2), an isostructural substitution process could occur between the FTO and R-TiO_2 with ions exchanges between Ti^{4+} and Sn^{4+}, as shown in **Figure 1**. Thereby, only R-TiO_2 can be induced to grow on the FTO surface, while two TiO_2 polymorphs (A-TiO_2 and R-TiO_2) are produced in the $TiCl_4$ reaction solution. The proposed isostructural substitution-induced growth mechanism can be confirmed with the following experimental results.

X-ray diffraction (XRD) and high-resolution transmission electron microscope (HRTEM) for both TiO_2 crystals obtained from the FTO surface and the resulting $TiCl_4$ reaction solution are conducted (**Figure 2**). For the TiO_2 film deposited on the FTO surface, the (110) peak at 27.4°, the (101) peak at 38.1°, and the (211) peak at 54.3° are observed for R-TiO_2 and the other appeared peaks as (110) at 26.6°, (200) at 37.8°, and (211) at 51.8° are associated with SnO_2 in the FTO. However, in XRD patterns of TiO_2 powder separated from $TiCl_4$ solution, not only the characteristic peaks for R-TiO_2 are noted, but also (101) and (200) peaks related to A-TiO_2 are presented. Therefore, it is clear that the growth of R-TiO_2 based on the same tetragonal system is dominant due to the reduced interface energy. As the isostructural substitution-induced growth mechanism is dependent on the similarity of crystalline structure and lattices, it can be sure that the different crystal facets of FTO can lead to different situations in the initial stage. Similar to the epitaxial growth of crystals, the induced growth of rutile TiO_2 should follow the same plane as the FTO. However, with the growth of the rutile TiO_2, the final situation is certainly dependent on the growth pattern of the rutile TiO_2 itself, keeping the lowest surface energy in a certain growth environment. As shown in XRD in Figure 2a, the rutile TiO_2 layer also shows the different crystal facets. However, it is not easy to identify the difference between the ion exchange and isostructural substitution in the different crystal planes due to the multicrystalline feature of FTO. In addition, the HRTEM image (from the transmission electron microscopy [TEM] images as shown in Figure S1, Supporting Information) for TiO_2 obtained from the $TiCl_4$ solution shows the interplanar spacing of 0.35 nm corresponding to the crystal plane (101) of A-TiO_2 (Figure 2d). However, in the HRTEM observations of TiO_2 formed on the FTO (Figure 2e), there are only interplanar spacing of R-TiO_2,

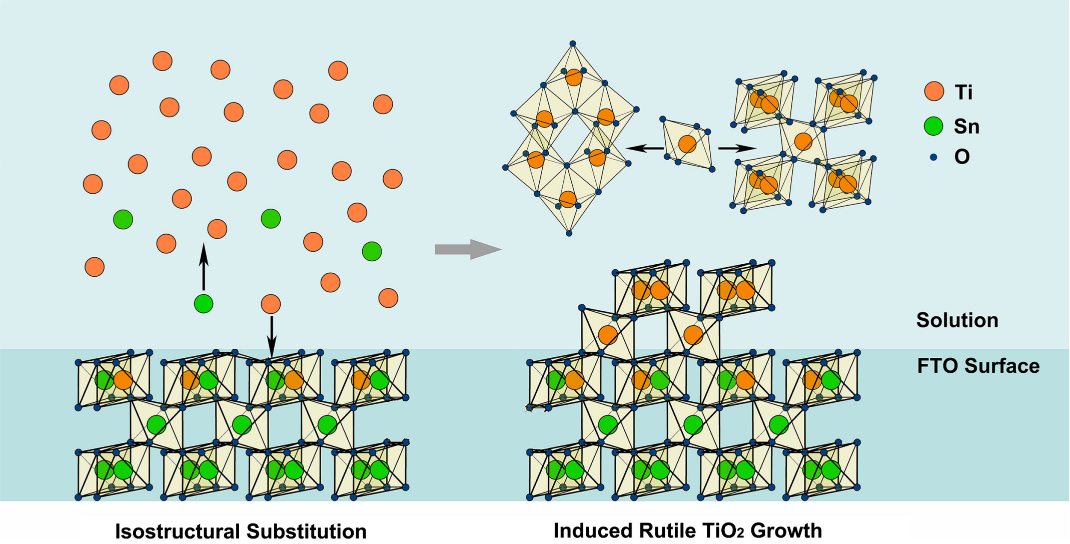

Figure 1. A schematic illustration: an isostructural substitution effect (ISE) inducing pure R-TiO_2 on FTO surface which is different with two phases TiO_2 hybrid in solution.

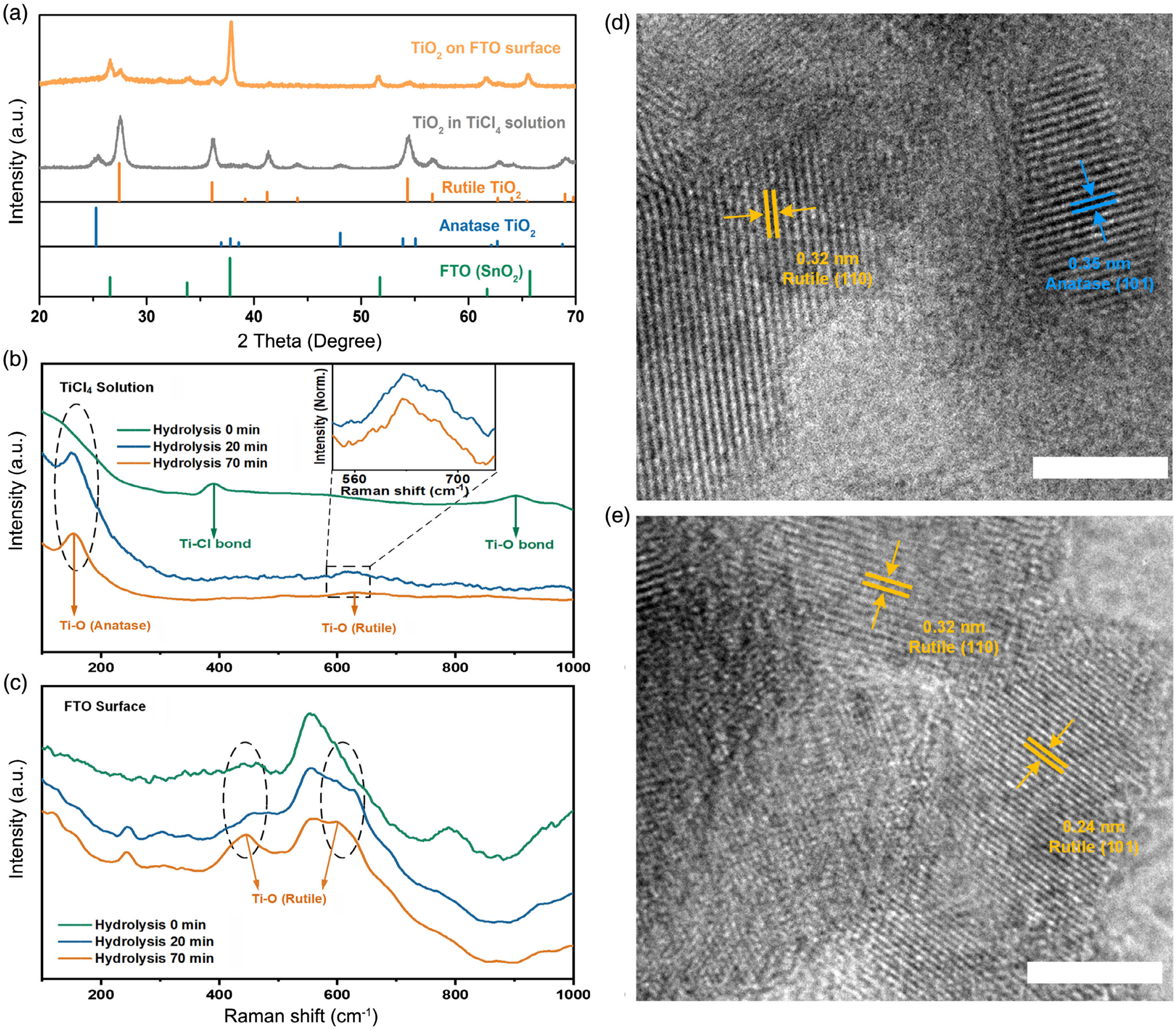

Figure 2. a) XRD pattern of R-TiO_2 film on FTO surface and hybrid-phase TiO_2 powders; b,c) Raman spectra of raw $TiCl_4$ aqueous solution and TiO_2 film on FTO hydrolysis with different (0, 20, and 70 min), respectively; d,e) HR-TEM images of hybrid-phase TiO_2 powders and R-TiO_2 powders scratched from FTO surface. The standard patterns of R-SnO_2 and R-TiO_2 draw from PDF#46-1088 and PDF#21-1276, respectively. Orange lines denote the orientation of rutile plane (110) and (101), corresponded with 0.32 and 0.24 nm respectively; Cyan lines orientate anatase plane (101) with distances of 0.35 nm; the white rectangle mark represents 5 nm.

e.g., 0.32 and 0.24 nm related to crystal plane (110) and (101) of R-TiO_2, respectively. To further identify the TiO_2 crystal phases and clarify the $TiCl_4$ hydrolysis process in solution and on FTO surface, we compare the Raman spectra for the $TiCl_4$ solution (Figure 2b) and FTO surface (Figure 2c) with different hydrolysis times (0, 20, and 70 min), respectively. For pristine $TiCl_4$ aqueous solution, the characteristic vibration peaks of the Ti—O and Ti—Cl bond located at 904.5 and 391.5 cm^{-1} are observed, respectively, indicating TiO_mCl_n complexes are generated with an incomplete substitution of Cl by O[18] in $TiCl_4$ precursor. As the hydrolysis time is set for 20 or 70 min, new vibration peaks prominently appear at 152.4 and 624.9 cm^{-1}, respectively, associated with the Ti—O in A-TiO_2 and R-TiO_2, and the former peaks (at 904.5 cm^{-1} and 391.5 cm^{-1}) disappear, which means the TiO_mCl_n complexes are mostly reacted to produce Ti—O ingredients for A-TiO_2 and R-TiO_2 crystals. Nevertheless, for the FTO surface, the peaks for R-TiO_2 are not noticeable while the vibration peaks featured at 447.5 and 601.7 cm^{-1} which are both corresponded to Ti—O in R-TiO_2 become more distinct when the hydrolysis time is increased. These results are consistent with XRD analyses and indicate the coexistence of A-TiO_2 and R-TiO_2 in solution but only R-TiO_2 is generated on the FTO surface. Therefore, it is clear that there is only R-TiO_2 generated on the FTO surface, while mixed crystals of anatase and rutile are formed in the resulting $TiCl_4$ solution.

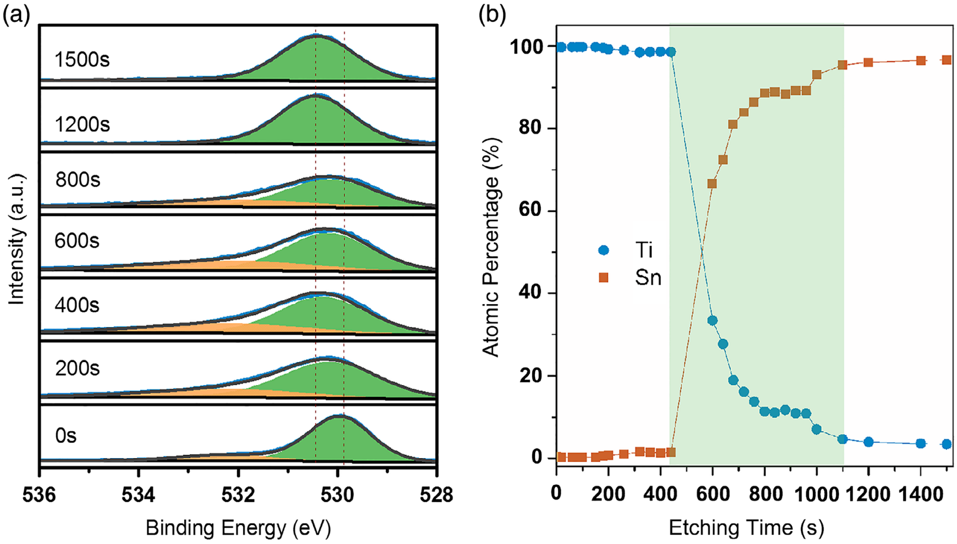

Figure 3. a) XPS spectra of O 1*s* at different etching time; b) atomic percentages between Ti-element and Sn-element by XPS depth profiling.

The isostructural substitution of Ti for Sn can be confirmed by analyzing the changes of the chemical state of oxygen at the interface using X-ray photoelectron spectroscopy (XPS) depth profiling measurements because the O 1*s* binding energy in TiO_2 is lower than that in FTO in the light of the identical crystal structure but the different elementary metallicity of Ti and Sn. **Figure 3**a shows the narrow scans of O 1*s* of an R-TiO_2 film on FTO with Ar^+ etching from 0 to 1500 s. Apart from the signal at 529.4–529.8 eV for lattice oxygen, there is a signal at higher than 531.0 eV, in particular in the early etching measurements. This is attributed to the formation of oxygen vacancies during the etching process.[19] Importantly, the binding energy of O 1*s* for lattice oxygen shows obvious shifts to a higher value with increasing etching time. Compared with the initial value of 529.3 eV, the binding energy of O 1*s* after etched for the 1500 s rises to 529.8 eV, revealing the chemical state change from Ti—O to Sn—O. But we note that the O 1*s* peaks are shifted in nonlinear with increasing the etching time, which is possibly attributed to the reduction of Ti and Sn by argon-ion during etching,[19a,19b] as shown in Figure S2, Supporting Information. The detailed analysis of the interface of R-TiO_2 and FTO is shown in Figure 3b. The relative atomic percentage of Ti presents a sharp decrease at the etching time around 500 s, suggesting the starting edge of the interface of R-TiO_2 and FTO. As the etching time is changed from 500 to 1150 s, the atomic percentage of the Ti element is close to zero. This process could be regarded as probing through the interface with a roughness of ≈20–80 nm for the FTO surface. In other words, the isostructural substitution of Ti for Sn occurs in the scale of tens of nanometers near the surface of FTO, which induces the formation of a pure R-TiO_2 layer on FTO.

The isostructural substitution means an ion exchange between Ti and Sn. To verify the ion exchange, rutile SnO_2 nanoparticles with a diameter around 50–70 nm are put in $TiCl_4$ aqueous solution and heated at 80 °C for 1 h. TEM-mapping images in Figure S3, Supporting Information, show that SnO_2 nanoparticles are fully covered by the synthesized TiO_2. Then the concentration of Sn in the resulting $TiCl_4$ solution is measured by inductively coupled plasma optical emission spectroscopy (ICP-OES). As shown in Table S1, Supporting Information, Sn has a concentration of 4.1 mg L^{-1} in the solution after the $TiCl_4$ hydrolysis on FTO. To avoid the influence of the highly concentrated hydrochloric acid (H–HCl) on FTO, a similar procedure is conducted on FTO but only using H–HCl with the same acidity. The Sn concentration in the consequent HCl solution (1.5 mg L^{-1}) is much less than that in the $TiCl_4$ solution, as shown in Table S1, Supporting Information. Therefore, the conclusion can be drawn that the part of Sn in FTO is replaced by Ti and is isolated to solutions during the $TiCl_4$ hydrolysis and the acid environment could accelerate the Sn dissolution but not as the main factor. It is very hard to precisely control the concentration of substituted Ti because any changes in the preparation conditions would influence the situation of the TiO_2 layer more than the concentration of the substituted Ti. Compared with the final situation of the rutile TiO_2, the influence of the substituted Ti concentration on the performance of PSCs should be very little. Furthermore, to demonstrate the essence of the conditions for particularly producing R-TiO_2 on the FTO surface, we used a titanium diisopropoxide bis(acetylacetonate) solution (≈75% in isopropanol) as the precursor to prepare the TiO_2 layer on the FTO substrate. As shown in Figure S4, Supporting Information, the XRD results show that only A-TiO_2 is grown on the FTO substrate, which is in agreement with kinds of literature,[20] suggesting that the isostructural Sn–Ti framework combined with a strong acid environment for $TiCl_4$ hydrolysis is the key to induce the R-TiO_2 growth on FTO surface.

Due to the complexity that multiple crucial intermediate states of $TiO_mCl_nH_l$ are generated and then rapidly disappear in the process, it must be admitted that the precise control for achieving a highly efficient PSC is still very difficult. Some of these unstable intermediate states have been reported by researchers.[21] Here, we try to map the relationship between the key experimental

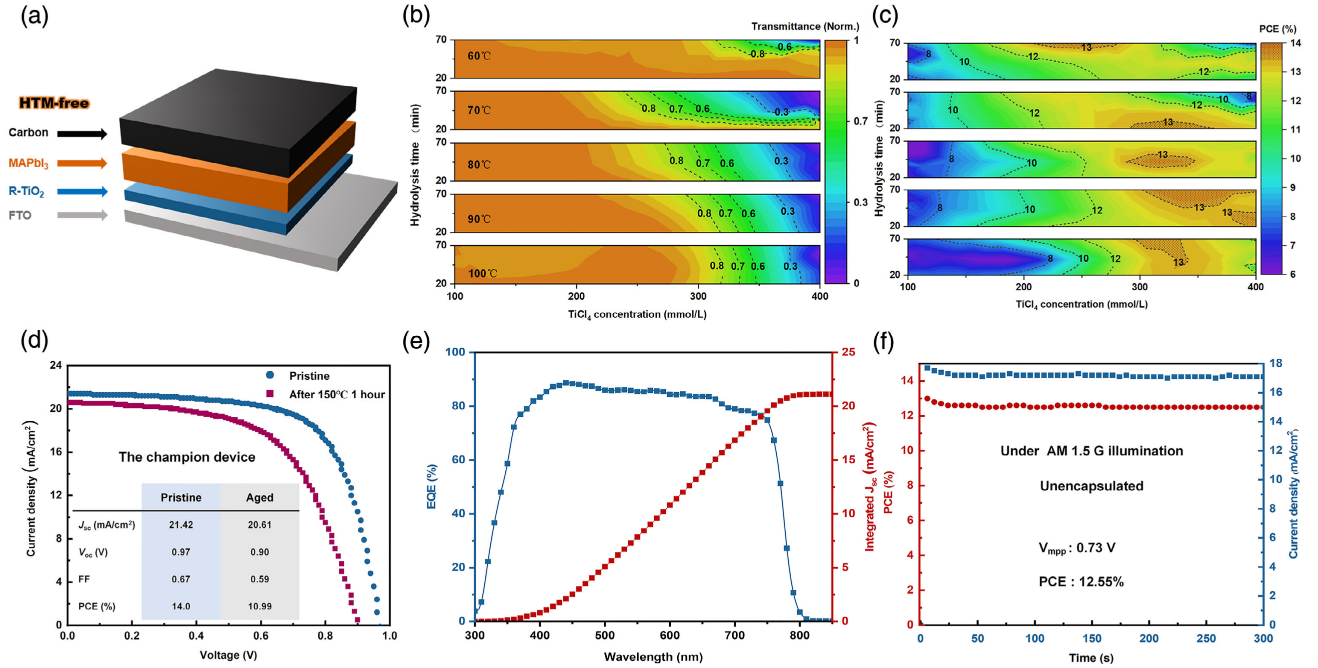

Figure 4. a) Schematic of HTL-free carbon-based planar perovskite solar cell; b,c) false-color mapping about transmittance and photovoltaic performance of devices in different condition prepared R-TiO_2; the transmittance was normalized from 0 to 1; d) the $J-V$ curve and photovoltaic performance of the champion device in ambient and experienced real temperature 150 °C in the nitrogen-filled glove box for 1 h, after a regular reverse scan, forward scan, and maximum power point test, respectively; e) the corresponding EQE spectrum of the champion device, showing an integrated J_{sc} of 21.11 mA cm^{-2}; f) the stabilized current density and PCE at the maximum power point (0.73 V) of the champion device tested under simulated sunlight AM1.5 G illumination with unencapsulated.

conditions of $TiCl_4$ hydrolysis, the properties of the resulting TiO_2 layers, and further the performance of the photovoltaic devices, to proceed with the dominant distribution in R-TiO_2 ETL preparation for a highly efficient PSC. The HTL-free carbon-based planar devices are fabricated using the structure of FTO/R-TiO_2/$MAPbI_3$/carbon schematically shown in **Figure** 4a. With careful consideration of the transmittance of R-TiO_2 ETL as the bottom and the only carrier-selective layer in the devices, first, we precisely controlled the reaction time and the precursor concentration during $TiCl_4$ hydrolysis to reveal the relationship between these parameters and the transmittance of the produced R-TiO_2. First things first, the FTO substrates are put in four differently concentrated $TiCl_4$ solutions (100, 200, 300, and 400 mmol L^{-1}) and were heated for 20 to 70 min at 60, 70, 80, 90, and 100 °C, respectively. Then, the transmittance for each condition of the R-TiO_2 layer was measured and presented in Figure S5, Supporting Information, as well as the resulting false-color transmittance spectral image is shown in Figure 4b. As the concentration of $TiCl_4$ solution and the reaction time are increased, the transmittance of R-TiO_2 is decreased because the thickness of the resulting TiO_2 films gets increased.[22] By comparing the transmittance of R-TiO_2 synthesized at different temperatures, it is clear that more concentrated $TiCl_4$ solutions are required to reach the same transmittance when the hydrolysis temperature is increased. The reason is that the increased temperature could accelerate the TiO_2 nucleation and growth in solutions rather than on the FTO surface, which leads to rapid consumption of Ti^{4+} in $TiCl_4$ solution, further resulting in slow growth of R-TiO_2 on the FTO surface and more Ti^{4+} sources are needed. But below 70 °C, the transmittance of TiO_2 is around 100% over large ranges of $TiCl_4$ concentration and reaction time because the rate of the TiO_2 growth is extremely low both for the solution and FTO surface. However, different transmittance of TiO_2 has few influences on the absorption of subsequently deposited perovskite films, as shown in Figure S6, Supporting Information.[2,23] It can be found that, although the transmittance of ETL is changed with the different preparation conditions, the transmittance of the films after the perovskite absorber deposited is very close. This is because the part of the perovskite absorber filling in the TiO_2 film still keeps the ability for absorbing light, as shown in Figure S6b, Supporting Information. Therefore, in a broad range, the decreased transmittance of ETL does not lead to a reduction in PSC's power conversion efficiency.

To seek the dominant distribution of R-TiO_2 ETL preparation for a highly efficient PSC, we utilize the TiO_2 films for each condition to fabricate the PSCs and measure the corresponding PCEs. A false-color PCE spectral image is obtained, as shown in Figure 4c. The PCEs of the fabricated PSCs are increased when the used concentrations of $TiCl_4$ precursor are increased, which is attributed to the increased R-TiO_2 film thickness with improved film compactness. As shown in Figure S7, Supporting Information, when the thin R-TiO_2 film covering the FTO cannot conceal the original morphology of the FTO, while the R-TiO_2 with the increased thickness, a more compact R-TiO_2 film can be observed in Figure S7b, Supporting Information. This is determined by the fundamental crystal growth theory that the high concentration is favorable for rapidly producing small TiO_2 nanocrystals and forming a compact film on FTO that can effectively reduce the interface charge recombination in PSCs. In general, the high PCEs above 13% are mainly delivered from the TiO_2 films that are produced using 300–400 mmol L^{-1} $TiCl_4$ precursor with the hydrolysis temperature above 70 °C. Combined with the analyses of the transmittance of TiO_2 in Figure 4b, it is noted that the appropriate range of R-TiO_2 transmittance for fabricating high-efficiency devices is around 60–80%. Interestingly, when the TiO_2 is synthesized at 60 °C with approximate 200–250 mmol L^{-1} of $TiCl_4$ concentration, after around 50 min of reaction time, the resulting film with about 100% of transmittance formed on FTO leads to the PCEs of devices surpass 13%, suggesting the obtained film is thin but compact enough for blocking hole transport in solar cells. Based on the delicate control of R-TiO_2 and device optimization, the PCE from the reverse scan of the HTL-free carbon-based PSCs is improved up to 14.0% under AM1.5G with J_{sc} of 21.42 mA cm^{-2}, V_{oc} of 0.97 V, and fill factor (FF) of 67.35%, as shown in Figure 4d. To verify the J_{SC}, the external quantum efficiency (EQE) was measured (Figure 4e). The corresponding forward scan is shown in Figure S8, Supporting Information. The stabilized power output is measured at a maximum power point (MPP) of 0.73 V for 300 s presenting an efficiency of 12.55% (Figure 4f). It is worth noting that the fabricated device with the champion PCE undergoes a heating process at 150 °C (measured for the top carbon contact of devices by an infrared thermometer) for 1 h in the nitrogen-filled glove box and retains about 80% of initial PCE (from 14.00% down to 10.99%) as shown in Figure 4d, indicating superior stability of FTO/R-TiO_2/$MAPbI_3$/carbon structure to extreme thermal conditions.

3. Conclusion

In this work, the special isostructural substitution-induced growth mechanism of TiO_2 on FTO by $TiCl_4$ hydrolysis is revealed to explain the selective deposition of rutile TiO_2 film on the FTO surface. In the range of tens of nanometres in the surface of FTO, the isostructural substitution of Ti for Sn occurs by ion exchange of both. The effect induces TiO_2 to grow along with the same rutile structure as FTO. Moreover, a dominant distribution of R-TiO_2 ETL preparation for HTL-free carbon-based planar PSCs is mapped with the key preparation conditions. The champion PCE reaches 14.0%, with J_{sc} of 21.42 mA cm^{-2}, V_{oc} of 0.97 V, and FF of 67.35% under reverse scanning. Moreover, after undergoing an extreme real temperature 150 °C heating test, the device represents excellent stability against thermal stress. The results provide remarkable universal and practical avenues to construct effective, low-cost, and stable HTL-free carbon-based PSCs, which is also inspirational to other solar cells and semiconductive film.

4. Experimental Section

Materials: Titanium tetrachloride ($TiCl_4$, $>98\%$) was purchased from Adamas-beta. Methylammonium iodide (MAI) and lead iodide (PbI_2) were purchased from Xi'an Polymer Light Technology Corp., China should be corrected as Advanced Election Technology Co., Ltd. Dimethylformamide (DMF), dimethyl sulfoxide (DMSO), and nanometer tin dioxide (SnO_2) were purchased from J&K Scientific, China. Low temperature carbon electrode paste was obtained from Shanghai MaterWin New Materials Co., Ltd. The 3M tape was Scotch and the sponge was CLEANWRAP.

Preparation and Fabrication: $TiCl_4$ solutions with the different concentrations of 100, 200, 300, and 400 mmol L^{-1} were obtained by adding dropwise quantitative 1 M $TiCl_4$ solution into ice water at 0 °C using a peristaltic pump (1.25 mL min^{-1}). The fluorine-doped tin oxide (FTO, 15 Ω cm^{-1}) was cleaned by sponge washing in flowing water and ultrasonic cleaning with isopropanol (IPA) for about 30 min sequentially. After that, a low-temperature plasma disposing was conducted for further cleaning FTO (300 W, 5 min). The cleaned FTO substrates were bathed into the $TiCl_4$ solution with a certain concentration adequately and heated at the designed temperature in the range of 60–100 °C on a temperature-controlled hotplate for 20–70 min. After kept for the specified time, the substrates were fetched out and fully rinsed with deionized water, and then immersed in ethanol. The obtained TiO_2/FTO plates were blown with nitrogen gas and annealed in a muffle furnace at 500 °C with a rising rate of 2 °C min^{-1} in the air atmosphere for 1 h. Finally, after cooled to room temperature, the obtained plates were transferred to a nitrogen glove box for the next step of fabrication of perovskite solar cells.

The perovskite absorber $MAPbI_3$ (MAI: 159 mg, PbI_2: 477 mg) in the solvent (DMF: 500 µL, DMSO: 145 µL) was spin-coated by two steps with 1000 rpm for 10 s (500 rpm s^{-1}) and 4000 rpm for 24 s (2000 rpm s^{-1}). Anisole (125 µL), green antisolvent, was quickly dropped at the tenth second after the second step commenced, and kept at 150 °C for 7 min in ambient air condition (humidity: 20–70%). Three strips of 3M tapes with a thickness of about 50 µm were pasted separately on the surface of the perovskite layer to divide into two narrow areas for obtaining two parallel cells. And the carbon paste was coated by the doctor blade method in the two narrow areas to form a carbon electrode with a thickness of about 5 µm. The active area was about 0.15 cm^2 and the testing mask area for the solar cells was 0.1 cm^2.

Characterization and Measurements: XRD was conducted on a Rigaku Smart Lab diffractometer using Cu Kα radiation as X-ray sources with 40 kV voltage and 40 mA current. The scanning mode and type were 2theta–theta and continuous scanning, respectively. TEM was conducted on a JEOL JEM-2800 machine. Transmittance spectra were collected using a UV–vis spectrophotometer (VARIAN CARY 100 Conc.). Raman spectra were measured on a Thermo Fisher (model Dxi) spectrometer with the range from 300 to 1000 nm under the excitation wavelength of 532 nm. ICP-OES was performed on an Agilent Model 730 machine. XPS was conducted on a Thermo SCIENTIFIC ESCALAB 250 Xi spectrometer using monochromatic Al Kα (1486.6 eV) radiation. The etching rate was around 0.1 nm s^{-1}. The samples were etched at a certain site, and the base pressure chamber was always around 2×10^{-9} mbar. The photocurrent density–voltage (*J–V*) characteristic curves of all the perovskite solar cells were obtained from Keithley 2612 Source Meter under AM1.5 G illumination (≈100 mW cm^{-2}) using a Newport/Oriel Sol 3A solar simulator. The light intensity was calibrated by a Newport/Oriel instruments PV reference cell system (model 91 150). The *J–V* measurements were conducted with a reverse scan ($-1.1 \rightarrow 0$ V) and a forward scan ($0 \rightarrow -1.1$ V) in air condition (≈22 °C, humidity: 20–70%) using a four-probe method. The MMP steady test was conducted in ambient air conditions. After that, the device was heated on the hotplate at a real temperature 150 °C (carbon surface) for 1 h in the nitrogen glove box and tested in ambient conditions for a high-temperature tolerance test. The EQE measurements were conducted in ambient air using a QE system (EnliTech) with monochromatic light of 20 Hz.

Supporting Information

Supporting Information is available from the Wiley Online Library or from the author.

Acknowledgements

This work was supported by the Natural Science Foundation of Tianjin (gran no. 18JCZDJC31000), NCC Fund (grant no. NCC2020PY01), the Fundamental Research Funds for the Central Universities, Nankai University (grant no. 63211043), and the China Postdoctoral Science Foundation (grant no. 2020M680861).

Conflict of Interest

The authors declare no conflict of interest.

Data Availability Statement

Research data are not shared.

Keywords

carbon-based planar perovskite solar cells, chemical bath deposition, electron transport layers, hole transport layer-free solar cells, rutile TiO_2

Received: April 27, 2021
Revised: July 1, 2021
Published online:

---

[1] a) Y. Rong, Y. Hu, A. Mei, H. Tan, M. I. Saidaminov, S. I. Seok, M. D. McGehee, E. H. Sargent, H. Han, *Science* **2018**, *361*, aat8235; b) A. Kojima, K. Teshima, Y. Shirai, T. Miyasaka, *J. Am. Chem. Soc.* **2009**, *131*, 6050; c) J. J. Yoo, G. Seo, M. R. Chua, T. G. Park, Y. Lu, F. Rotermund, Y. K. Kim, C. S. Moon, N. J. Jeon, J. P. Correa-Baena, V. Bulovic, S. S. Shin, M. G. Bawendi, J. Seo, *Nature* **2021**, *590*, 587; d) C. Zuo, H. J. Bolink, H. Han, J. Huang, D. Cahen, L. Ding, *Adv. Sci.* **2016**, *3*, 1500324.

[2] A. Mei, X. Li, L. Liu, Z. Ku, T. Liu, Y. Rong, M. Xu, M. Hu, J. Chen, Y. Yang, M. Gratzel, H. Han, *Science* **2014**, *345*, 295.

[3] a) M. Cai, Y. Wu, H. Chen, X. Yang, Y. Qiang, L. Han, *Adv. Sci.* **2017**, *4*, 1600269; b) S. Chu, Y. Cui, N. Liu, *Nat. Mate.* **2016**, *16*, 16; c) L. Qiu, S. He, L. K. Ono, S. Liu, Y. Qi, *ACS Energy Lett.* **2019**, *4*, 2147; d) Y. Zhu, L. Shu, Z. Fan, *Chem. Res. Chin. Univ.* **2020**, *36*, 366.

[4] a) M. Chen, Q. Zhang, L. Wan, Y. Gan, Z. Liu, Y. Wang, Y. Liu, J. Wang, F. Chen, D. Eder, S. Wang, *Sol. Energy* **2018**, *170*, 1087; b) X. Liu, X. Tan, Z. Liu, H. Ye, B. Sun, T. Shi, Z. Tang, G. Liao, *Nano Energy* **2019**, *56*, 184; c) X. Liu, Z. Liu, B. Sun, X. Tan, H. Ye, Y. Tu, T. Shi, Z. Tang, G. Liao, *Electrochim. Acta* **2018**, *283*, 1115; d) M. Cheng, C. Zuo, Y. Wu, Z. Li, B. Xu, Y. Hua, L. Ding, *Sci. Bull.* **2020**, *65*, 1237.

[5] a) M. Jeong, I. W. Choi, E. M. Go, Y. Cho, M. Kim, B. Lee, S. Jeong, Y. Jo, H. W. Choi, J. Lee, J. H. Bae, S. K. Kwak, D. S. Kim, C. Yang, *Science* **2020**, *369*, 1615; b) B. O'Regan, M. Grätzel, *Nature* **1991**, *353*, 737; c) Q. Zhao, A. Hazarika, X. Chen, S. P. Harvey, B. W. Larson, G. R. Teeter, J. Liu, T. Song, C. Xiao, L. Shaw, M. Zhang, G. Li, M. C. Beard, J. M. Luther, *Nat. Commun.* **2019**, *10*, 2842; d) C. Xiao, Q. Zhao, C.-S. Jiang, Y. Sun, M. M. Al–Jassim, S. U. Nanayakkara, J. M. Luther, *Nano Energy* **2020**, *78*, 105319; e) J. Peng, D. Walter, Y. Ren, M. Tebyetekerwa, Y. Wu, T. Duong, Q. Lin, J. Li, T. Lu, M. A. Mahmud, O. L. C. Lem, S. Zhao, W. Liu, Y. Liu, H. Shen, L. Li, F. Kremer, H. T. Nguyen, D.-Y. Choi, K. J. Weber, K. R. Catchpole, T. P. White, *Science* **2021**, *371*, 390; f) Y. Xiang, J. Zhuang, Z. Ma, H. Lu, H. Xia, W. Zhou, T. Zhang, H. Li, *Chem. Res. Chin. Univ.* **2019**, *35*, 101.

[6] a) M. Shahiduzzaman, S. Visal, M. Kuniyoshi, T. Kaneko, S. Umezu, T. Katsumata, S. Iwamori, M. Kakihana, T. Taima, M. Isomura, K. Tomita, *Nano Lett.* **2019**, *19*, 598; b) P. Chen, G.-R. Li, T.-T. Li, X.-P. Gao, *Adv. Sci.* **2019**, *6*, 1900620; c) P. Chen, T.-T. Li, G.-R. Li, X.-P. Gao, *Sci. China Mater.* **2020**, *63*, 1693.

[7] a) X. Liu, M. Afzaal, K. Ramasamy, P. O'Brien, J. Akhtar, *J. Am. Chem. Soc.* **2009**, *131*, 15106; b) K. Govender, D. S. Boyle, P. O'Brien, D. Binks, D. West, D. Coleman, *Adv. Mater.* **2002**, *14*, 1221.

[8] A. Yella, L.-P. Heiniger, P. Gao, M. K. Nazeeruddin, M. Grätzel, *Nano Lett.* **2014**, *14*, 2591.

[9] Y. Wang, J. Wan, J. Ding, J.-S. Hu, Dan. Wang, *Angew. Chem. Int. Ed.* **2019**, *58*, 9414.

[10] J. He, E. Bi, W. Tang, Y. Wang, X. Yang, H. Chen, L. Han, *Nanomicro Lett.* **2018**, *10*, 49.

[11] a) K.-H. Hu, Z.-K. Wang, K.-L. Wang, M.-P. Zhuo, Y. Zhang, F. Igbari, Q.-Q. Ye, L.-S. Liao, *Sol. RRL* **2019**, *3*, 1900201; b) Y. Zhao, Z. Han, W. Zhou, Q. Li, R. Fu, D. Yu, Q. Zhao, *Sol. RRL* **2019**, *3*, 1900167.

[12] a) D. Bogachuk, S. Zouhair, K. Wojciechowski, B. W. Yang, V. Babu, L. Wagner, B. Xu, J. Lim, S. Mastroianni, H. Pettersson, A. Hagfeldt, A. Hinsch, *Energy Environ. Sci.* **2020**, *13*, 3880-3916; b) T.-T. Li, Y.-B. Yang, G.-R. Li, P. Chen, X.-P. Gao, *Small* **2021**, 2006145.

[13] a) R. D. Shannon, J. A. Pask, *J. Am. Ceram. Soc.* **1965**, *48*, 391; b) D. Reyes-Coronado, G. Rodríguez-Gattorno, M. E. Espinosa-Pesqueira, C. Cab, R. de Coss, G. Oskam, *Nanotechnology* **2008**, *19*, 145605.

[14] S.-D. Mo, W. Y. Ching, *Phys. Rev. B* **1995**, *51*, 13023.

[15] Yi. Hu, H.-L. Tsai, C.-L. Huang, *J. Eur. Ceram. Soc.* **2003**, *23*, 691.

[16] a) H. Y. Zhu, Y. Lan, X. P. Gao, S. P. Ringer, Z. F. Zheng, D. Y. Song, J. C. Zhao, *J. Am. Chem. Soc.* **2005**, *127*, 6730; b) H. Yin, Y. Wada, T. Kitamura, S. Kambe, S. Murasawa, H. Mori, T. Sakata, S. Yanagida, *J. Mater. Chem.* **2001**, *11*, 1694.

[17] a) T. Sasaki, S. Nakano, S. Yamauchi, M. Watanabe, *Chem. Mater.* **1997**, *9*, 602; b) Z. Wang, S. Zhou, L. Wu, *Adv. Funct. Mater.* **2007**, *17*, 1790.

[18] Q. Zhang, J. Luan, X. Huang, Q. Wang, D. Sun, Y. Tang, X. Ji, H. Wang, *Nat. Commun.* **2020**, *11*, 3961.

[19] a) S. A. Abdullah, M. Z. Sahdan, N. Nayan, Z. Embong, C. R. C. Hak, F. Adriyanto, *Mater. Lett.* **2020**, *263*, 127143; b) Y. Sakai, S. Ninomiya, K. Hiraoka, *Surf. Interface Anal.* **2012**, *44*, 938; c) J. Rumble, D. Bickham, C. Powell, *Surf. Interface Anal.* **1992**, *19*, 241; d) L. Gao, Y. Yan, Y. Li, T. Ma, *Chem. Res. Chin. Univ.* **2020**, *36*, 1279.

[20] a) C. Yang, M. Yu, D. Chen, Y. Zhou, W. Wang, Y. Li, T. C. Lee, D. Yun, *Chem. Commun.* **2017**, *53*, 10882; b) J.-W. Lee, T.-Y. Lee, P. J. Yoo, M. Grätzel, S. Mhaisalkar, N.-G. Park, *J. Mater. Chem. A* **2014**, *2*, 9251.

[21] a) T.-H. Wang, A. M. Navarrete-Lopez, S. Li, D. A. Dixon, J. L. Gole, *J. Phys. Chem. A* **2010**, *114*, 7561; b) M. Rigo, P. Canu, L. Angelin, G. Della Valle, *Ind. Eng. Chem. Res.* **1998**, *37*, 1189; c) J. Sun, L. Gao, Q. Zhang, *J. Am. Ceram. Soc.* **2003**, *86*, 1677; d) S.-J. Kim, S.-D. Park, Y. H. Jeong, S. Park, *J. Am. Ceram. Soc.* **1999**, *82*, 927; e) C. Kormann, D. Bahnemann, M. Hoffmann, *J. Phys. Chem.* **1988**, *92*, 5196.

[22] D. F. Swinehart, *J. Chem. Educ.* **1962**, *39*, 333.

[23] J. H. Noh, S. H. Im, J. H. Heo, T. N. Mandal, S. I. Seok, *Nano Lett.* **2013**, *13*, 1764.